ROYAL SOCIETY
OF CHEMISTRY

PAPER

Check for updates

Coating dynamics in two-step hybrid evaporated/blade-coated perovskites for scalable fully-textured perovskite/silicon tandem solar cells†

Oussama Er-raji, [ID] *[ab] Ahmed A. Said,[c] Anand S. Subbiah, [ID] [c]
Vladyslav Hnapovskyi, [ID] [c] Badri Vishal,[c] Anil R. Pininti,[c] Marco Marengo, [ID] [c]
Martin Bivour,[a] Markus Kohlstädt,[ad] Juliane Borchert, [ID] [ab] Patricia S. C. Schulze,[a]
Stefaan De Wolf [ID] [c] and Stefan W. Glunz[ab]

Perovskite/silicon tandem solar cells hold great promise for wide-scale photovoltaic deployment. Despite the achievement of high power conversion efficiencies (PCEs) exceeding 33%, the commonly used spin-coating technique for perovskite deposition encounters substantial scalability challenges. To address this, we investigate the potential of the two-step hybrid evaporation/blade-coating method for perovskite manufacturing on silicon with industry-standard texturing. Combining experimental results with theoretical considerations on meniscus formation, we comprehensively analyze the influence of fluid mechanisms involved in the blade-coating process and find that the final perovskite film properties can be controlled through two main properties: wet film thickness and solvent's evaporation rate. Furthermore, the study finds that unlike one-step blade-coated perovskites, where increased speed results in a U-shaped, speed-dependent thickness for evaporation and Landau–Levich coating regimes, the hybrid evaporation/blade-coating method reveals a different S-shaped curve, correlating speed with perovskite conversion rate. Good perovskite properties of fully-textured perovskite/silicon tandem solar cells are demonstrated by open-circuit voltages exceeding 1900 mV and a PCE approaching 28%. This work identifies key challenges in scalable perovskite deposition with the hybrid method, deriving learnings that can be transferred to other meniscus-based hybrid industrial techniques, and reinforces the need for film optimization with scalable methods at the early R&D stage.

Broader context

Monolithic perovskite/silicon tandem solar cells are highly attractive due to their potential to deliver high power conversion efficiencies at affordable costs. The fully-textured tandem architecture, where the perovskite absorber conformally coats textured silicon, has garnered particular attention recently for two primary reasons: (1) its enhanced optical design, which minimizes reflection losses, and (2) its compatibility with existing silicon production lines, which typically produce textured silicon substrates with micrometer-sized random pyramids. However, a key challenge to the commercial viability of this technology lies in the use of scalable techniques for the deposition of the perovskite absorber. To date, this process has predominantly relied on the two-step hybrid evaporation/spin-coating method. To address this challenge, this study investigates the coating dynamics of the scalable hybrid evaporation/blade-coating method for conformal perovskite growth on textured silicon. Considering the physics of meniscus formation, our experimental findings indicate that the features of the perovskite film can be fine-tuned by controlling two fundamental properties: the wet film thickness and the solvent's evaporation rate. Through meticulous control of the coating parameters during the blade-coating step, and using a solution volume which is eight times lower than that in spin-coating, fully-textured tandems achieved high open-circuit voltages exceeding 1900 mV.

[a]Fraunhofer Institute for Solar Energy Systems ISE, Heidenhofstr. 2, 79110 Freiburg, Germany. E-mail: oussama.er-raji@ise.fraunhofer.de

[b]Chair of Photovoltaic Energy Conversion, Department of Sustainable Systems Engineering (INATECH), University of Freiburg, Emmy-Noether-Strasse 2, 79110 Freiburg, Germany

[c]Center for Renewable Energy and Storage Technologies (CREST), Physical Sciences and Engineering, Division (PSE), King Abdullah University of Science and Technology, Thuwal 23955-6900, Kingdom of Saudi Arabia

[d]Materials Research Center FMF, University of Freiburg, Stefan-Meier-Straße 21, 79104 Freiburg, Germany

† Electronic supplementary information (ESI) available. See DOI: https://doi.org/10.1039/d5el00073d

1. Introduction

After successfully demonstrating lab-scale, highly-efficient perovskite/silicon tandem solar cells, the next step towards commercialization is demonstrating their scalability and long-term stability.[1–3] In one of the most promising manufacturing approaches, silicon bottom cells with industry-standard texturing are employed in combination with a perovskite absorber processed *via* a two-step, hybrid evaporation/wet-chemical method. This method involves the reaction between

thermally evaporated inorganic precursors with wet-chemically deposited organohalides during an annealing step, enabling conformal perovskite coating on large silicon pyramids (height > 1 µm). As a result, the fully-textured tandem architecture effectively minimizes reflection losses, thus offering high energy yield in the field.[4–8] To date, process development has been majorly carried out with spin-coating as the second wet-chemical step.[9–14] By tackling issues such as controlling crystallization for large grain size formation, elimination of residual PbI$_2$, passivation of perovskite bulk and interfaces, and development of compatible functional layers, fully-textured tandems achieved power conversion efficiencies (PCEs) exceeding 31%.[15–18] Nevertheless, the spin-coating step cannot offer a homogeneous deposition of coating solution on large areas, and the material wastage is high.

Due to its industrial compatibility and low material consumption, Zheng *et al.* proposed the use of blade-coating as an effective wet-chemical second step in the hybrid route.[19] By studying the impact of the solvent's polarity and saturation vapor pressure, the authors identified *n*-butanol as an optimal solvent for uniform and homogeneous film fabrication in air, leading to tandem solar cells with 28.8% stabilized PCE.[19]

Despite the promise of blade-coating in the hybrid route, several challenges impede further development, with the primary issue being understanding the dynamics of perovskite crystallization. For instance, we note that during spin-coating of organohalides on the inorganic scaffold, the crystallization is relatively fast owing to the axisymmetric gas flow caused by the rotation motion of the substrate, which speeds up solvent evaporation. Meanwhile, blade-coating the solution on the scaffold forces a prolonged solvent exposure, thus promoting extended solvent-precursor-intermediate phase interactions, thereby retarding crystallization. Considering the solvent system, properties such as (1) the boiling point should be optimized to avoid uncontrolled deposition patterns such as coffee rings, resulting from a slow drying process, (2) the viscosity and surface tension should be tuned to ensure good wetting for coating uniform thin films, and (3) the toxicity of the solvent should be minimized to reduce the environmental and human health impact of coating processes.[20]

Another typical parameter involved in blade-coating is the application of an air knife used to remove solvents from the drying wet films.[21–24] Variables such as the blowing strength of the air knife and the uncontrollable removal time render these films highly susceptible to inhomogeneities.[25,26] This issue is particularly pronounced during the fabrication of perovskites *via* hybrid methods, where low boiling point solvents are used, potentially leading to uneven crystallization across the substrate. Furthermore, the blade-coating process is sensitive to the blade-to-substrate gap, blade speed, and applied volume of solution, which dictate the dynamic meniscus properties and wet-film thickness. The substrate temperature also plays a critical role in the crystallization kinetics. Although in the case of one-step blade-coated perovskites, the blade speed was found to influence the wet film thickness, which in turn dictates the final perovskite film thickness,[27–29] and the substrate temperature was utilized to facilitate crystallization,[30,31] the impacts of these critical parameters remain ambiguous within the framework of the hybrid evaporation/blade-coating route, particularly on textured silicon substrates.

To address these challenges, through a targeted design of experiments we perform an in-depth investigation of seven parameters involved in the blade-coating step of the hybrid method, which have a significant potential to influence the device performance. The investigations are all carried out on textured silicon substrates with industry-relevant random pyramid texturing to replicate similar perovskite growth as in tandem solar cells. We find that learnings from spin-coating cannot be directly transferred to blade-coating due to the difference in crystallization dynamics, which urges film optimization using scalable techniques at the early development stage. With blade-coating, the solvent's evaporation rate and wet film thickness are identified as the main leverages to control perovskite film properties, and a close link to the different process parameters is established. This enables us to set up a standard operation procedure for a scalable two-step deposition of methylammonium-free perovskite with 1.68 eV bandgap, which yields tandem solar cells with an open-circuit voltage of 1903 mV and an efficiency approaching 28%. This research underlines the importance of understanding the causality of process parameters in enhancing perovskite photovoltaic performance and provides insights on perovskite film formation that can be used to develop other scalable, meniscus-based, hybrid deposition techniques.

2. Results and discussion

The hybrid evaporation/blade-coating route was used to conformally deposit perovskite layers with a bandgap of 1.68 eV on top of textured silicon. Specifically, CsBr and PbI$_2$ were thermally co-evaporated with a total scaffold thickness of 550 nm. Then, an organohalide mixture of FABr and FAI (FA denotes formamidinium) in a green solvent was blade-coated onto the scaffold to drive inorganic/organic precursor intermixing. Urea was added as a crystallization agent in the organohalide solution.[32,33] Finally, an annealing step was carried out at 100 °C in air (relative humidity of 40–50%) to complete perovskite film formation. The detailed fabrication method is described in the Experimental section (ESI†) and Fig. 1 illustrates the procedure. Perovskite/silicon tandem solar cells hold great promise for wide-scale photovoltaic deployment.

Following an initial review and analysis of various parameters that could influence perovskite film formation by the second wet-chemical blade-coating step, seven parameters were chosen for systematic investigation. These include solvent, solution concentration, solution volume, coating speed, coating gap, N$_2$ pressure, and stage temperature. For each parameter a thorough morphological, structural, and optoelectronic analysis of the perovskite film was performed.

2.1 Influence of solvent, solution concentration, and gas quenching on the perovskite crystallization

We first investigated the direct transferability of the solvent system used in the hybrid evaporation/spin-coating method
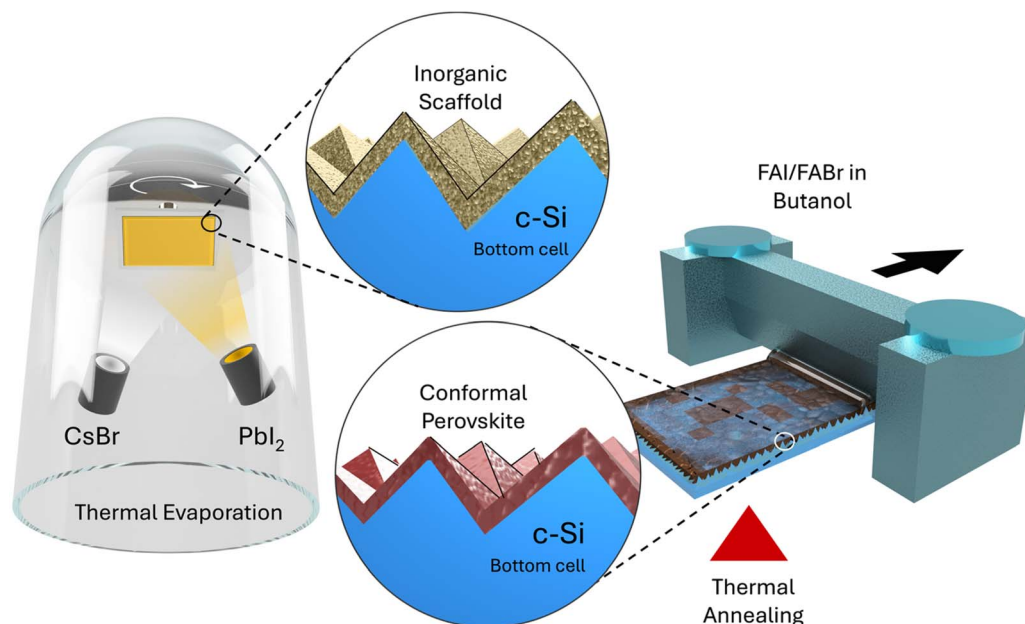
Fig. 1 Schematic illustrating the hybrid evaporation/blade-coating route for scalable perovskite film manufacturing on textured silicon solar cells. The blade-coating step is carried out in the glovebox and the thermal annealing step is carried out after that in air.
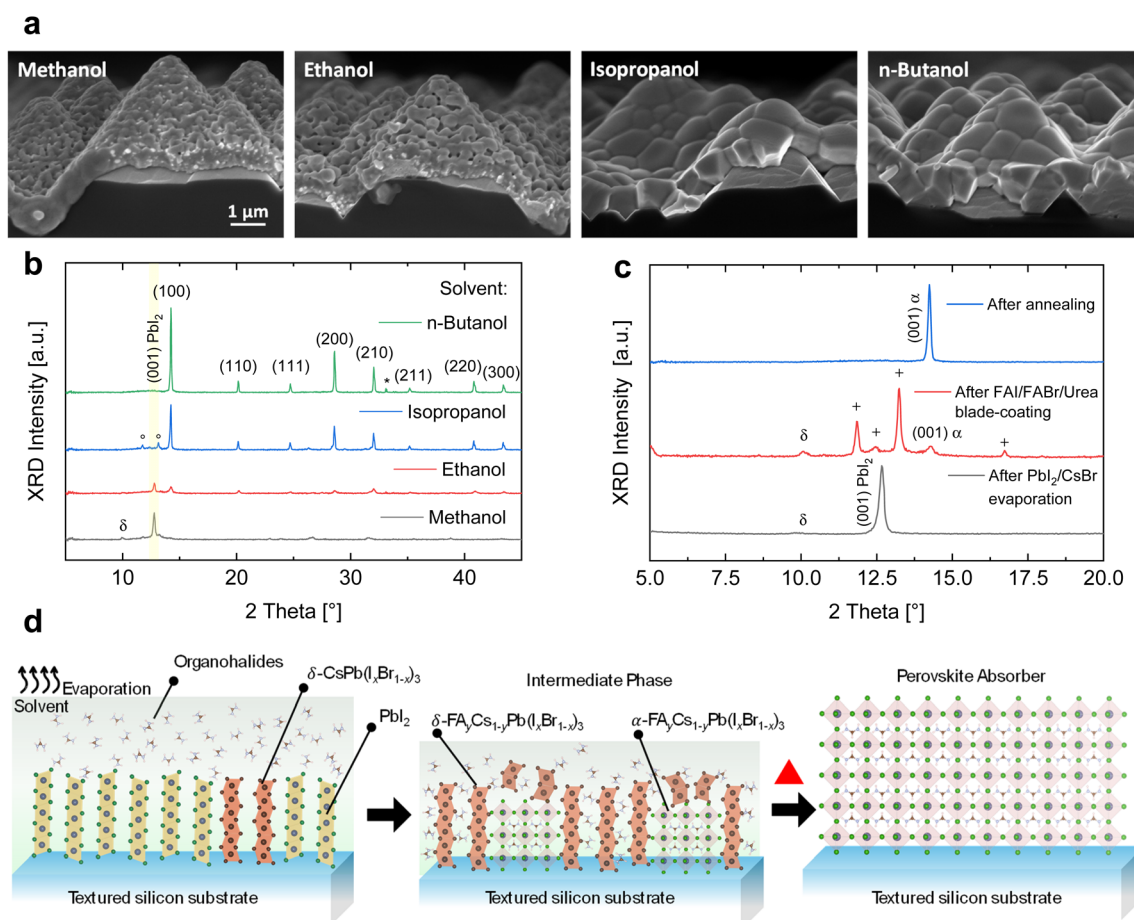

Fig. 2 Impact of solvent on the perovskite's morphological and structural properties, and crystallization in hybrid evaporation/blade-coating. (a) SEM images, and (b) XRD data of perovskite films fabricated with a variation in the solvent (* Si (002), δ-perovskite, ° additional phases). The probed stacks are based on textured silicon/ITO/Me-4PACz/perovskite and the solution concentration used is 0.8 M. (c) XRD data of films at different stages of the fabrication process with n-butanol as the solvent (+ intermediate phase). (d) Schematic of the phase transformations at different stages of the hybrid evaporation/blade-coating method.

(ethanol). Cross-sectional SEM images in Fig. 2a showed that the use of ethanol as the solvent typically employed in spin-coating, led to poor film morphology in blade-coating, with a high density of nm-scaled pinholes at the surface and film inhomogeneities. Furthermore, structural investigation *via* XRD revealed a low intensity diffraction pattern (low crystalline quality) and presence of remnant PbI_2 as denoted by the (001) reflex at 12.69° (highest intensity) (Fig. 2b). This phase impurity originates from incomplete inorganic scaffold to perovskite conversion. The presence of PbI_2 not only impedes charge transfer across the perovskite/bottom charge transport layer interface owing to its insulating nature, but it also is a leading cause for degradation.[34,35] The presence of pinholes and incomplete conversion can cause shunts and high series resistance in the device, respectively. By employing the typical conversion-tuning method based on increasing the organohalide solution concentration, a gradual elimination of PbI_2 is possible but the perovskite morphology remains dominated by pinholes (Fig. S1, ESI†).

By scanning different green alcohol solvents, the perovskite morphological quality was drastically altered. Particularly, using isopropanol and *n*-butanol, perovskite films demonstrated homogeneous film formation, without the presence of pinholes, and with large apparent grain size formation, ranging from 200 nm to > 1 μm (Fig. 2a). Moreover, XRD measurements highlighted a gradual change in structural phase composition from PbI_2-dominated with methanol and ethanol to perovskite-dominated with high crystallinity with isopropanol and *n*-butanol. Note that with isopropanol, additional unidentified crystalline phases occurred as denoted with ° in Fig. 2b.

Considering the different solvent properties, we correlated the change in conversion rate to changes in the boiling point of the solvent (Table 1). At low boiling point, solvents such as methanol (64.7°) evaporate relatively quickly, resulting in organic precursor crystallization on the scaffold surface. Conversely, solvents with high boiling point such as *n*-butanol (117.1 °C) extend the solution–scaffold interaction, enabling a complete perovskite conversion (Fig. S2, ESI†). With the optimal *n*-butanol solvent, it should be noted that the organohalide solution concentration must still be optimized to ensure full conversion (Fig. S3a, ESI†).

Interestingly, by carrying out a similar solvent variation with the conventional hybrid evaporation/spin-coating method, an opposite behavior was manifested (Fig. S4, ESI†). With increasing boiling point of the solvent, the perovskite conversion was deteriorated. To understand the differences in perovskite conversion between blade-coating and spin-coating in the hybrid route, the dynamics of solute transport in a solvent throughout a porous medium, described by Stokes–Einstein's equation, should be considered as indicated in eqn (1):

$$D = \frac{k_B T}{6\pi\mu R_0} \tag{1}$$

where D is the diffusion coefficient, k_B is the Boltzmann constant, T is the temperature, μ is the viscosity, and R_0 is the solute's radius. At a fixed temperature (room temperature in this experiment) and common solute size (FAI, FABr, urea), eqn (1) indicates that increasing the fluid's viscosity results in a reduction of the solute's diffusion coefficient across the porous medium (this inversely proportional relationship is similarly deducted following Darcy's law as described in Section 1, ESI†). Translating that to the hybrid method, solvents with higher viscosity, such as isopropanol and *n*-butanol (Table 1) impede the organohalide infiltration throughout the scaffold, thus rationalizing the deteriorated conversion in spin-coating. This observation only holds true in spin-coating given the fast solvent removal caused by the axisymmetric gas flow during rotation (2200 rpm used in our study). In contrast, owing to the absence of gas quenching in the blade-coating step, the high boiling point solvents extend the solution-scaffold interaction and thus lead to a complete perovskite conversion (unlike *e.g.*, methanol or ethanol that evaporate quickly despite their low viscosity). Overall, the result of this investigation agrees with the work of Zheng *et al.* who also identified *n*-butanol as the optimum solvent due to its polarity and saturation vapor pressure.[19] Here, we stress the importance of boiling point (also related to vapor pressure) as a crucial property to consider for solvent selection.

To get more insights into the processes of nucleation and crystal growth in the hybrid evaporation/blade-coating method, XRD measurements were carried out at different fabrication steps using the optimum solvent *n*-butanol (Fig. 2c). The scaffold evaporation revealed a dominant crystalline PbI_2 phase, denoted with the peak at 12.69°. Additionally, a peak at $2\theta = 10.0°$ pointed out the formation of a δ-perovskite phase, which is the $CsPb(I_xBr_{1-x})_3$ phase.[13,15] Following the organohalide solution deposition *via* blade-coating, the PbI_2 peak disappeared, the δ-perovskite phase was enhanced (due to incorporation of FAI & FABr), and a peak at 14.28° emerged, denoting the perovskite photoactive phase. These changes underlined fast crystallization dynamics, ascribed to the use of urea,[33] and indicated the presence of nucleation and crystal growth processes simultaneously prior to the annealing step.

We note here that for these fast crystallization dynamics to take place, it is imperative for urea to infiltrate the reaction site, *i.e.* the scaffold. This can be done, as described earlier, using a high boiling point solvent that enables an extended interaction time, driving organic precursors throughout the depth of the PbI_2/CsBr film. Once the solution has fully infiltrated the scaffold, urea functions as a crystallization agent, lowering the energy barrier for forming the α-perovskite phase.[33] After the blade-coating step, XRD measurements additionally show that the δ-perovskite phase remained present and that intermediate crystalline phases, primarily consisting of FAI, urea, PbI_2 and CsBr,[33] emerged (Fig. 2c). The final annealing step enabled

Table 1 Solvent boiling point and viscosity properties

	Methanol	Ethanol	Isopropanol	*n*-Butanol
Boiling point (°C)	64.7	78.4	82.3	117.1
Viscosity (mPa s⁻¹)	0.406	0.673	1.052	1.428

a complete transformation of intermediate phases to the perovskite photoactive phase. Similar to the hybrid evaporation/spin-coating route, annealing in air with high humidity (RH = 50%) enhanced the perovskite's final film properties compared to annealing in inert atmosphere (Fig. S5, ESI†).[36] The phase transformations with the hybrid evaporation/blade-coating method are depicted in Fig. 2d.

In a second step, we investigated the role of the N₂-knife, typically used to remove the solvent.[25,26] By introducing a 20 pound-force per square inch (PSI) N₂-pressure post solution coating, perovskite films exhibited reduced crystallinity and higher density of residual PbI₂ (Fig. S6, ESI†). This observation held true across different solvent systems (Fig. S6, ESI†), thus confirming the negative effect of gas-quenching in the hybrid route. Moreover, increasing the pressure beyond 20 PSI resulted in further deterioration of the perovskite conversion (Fig. S7, ESI†).

By comparing the effects of pressure and solvent, we derive a common mechanism that impacts the perovskite conversion rate, that is: accelerating the solvent's evaporation rate, either *via* selection of low boiling point solvents or *via* incorporation of gas-quenching through an N₂-knife, reduces the reaction time, thus preventing a complete organohalide infiltration along the inorganic scaffold and limiting the conversion. It is interesting to note that this result is in contradiction to that in one-step blade-coated perovskites where an air knife is typically applied after the deposition of perovskite ink solution to facilitate solvent evaporation, which drives supersaturation of the precursor film, and results in uniform nucleation/crystal growth.[24,37]

2.2 Influence of blade speed, solution volume, and stage temperature on the perovskite crystallization

After identifying the role of the solvent system, solution concentration, and N₂-knife application, we then study how perovskite crystallization dynamics are influenced by blade-coating speed, dispensed volume, and coating-stage temperature. We first probed the speed by varying it from 5 mm s⁻¹ to 50 mm s⁻¹ while maintaining a fixed volume of 20 μL at room temperature (for a substrate size of 2.5 × 2.5 cm²). The morphological, optoelectronic, and structural properties of perovskite films were assessed *via* SEM, hyperspectral PL imaging, and XRD (Fig. 3).

At low coating speed (5 mm s⁻¹), the perovskite film was characterized by a high surface roughness and small grain size as observed in cross-sectional SEM (Fig. 3a). Furthermore, the film exhibited a high density of residual PbI₂ as detected in XRD (Fig. 3b). This was reflected in an inhomogeneous PL response with multiple dark spots across the substrate as shown in spatially-resolved PL images (Fig. 3c). With increased coating speed and up to an optimum of 20 mm s⁻¹, the perovskite conversion rate improved, together with an enhancement of the photoactive phase's crystallinity, thus translating to a higher intensity of the perovskite's PL signal and an improved spatial homogeneity. Beyond 20 mm s⁻¹, the PL intensity was reduced (Fig. S8, ESI†) owing to the emergence of the δ-perovskite phase (denoted by XRD peaks at 2θ = 10.6°) and the decrease of crystallinity of the perovskite photoactive phase.

To understand the origin of enhanced perovskite phase purity with increased blade-coating speed, the two meniscus-modulated coating regimes – evaporation and Landau–Levich – should be considered.[38] The evaporation regime governs the coating process at low blade speeds where the drying timescale is comparable to the blade speed. Since the solvent evaporates as soon as the blade leaves away from the liquid-substrate surface, solute accumulation and solid film formation take place right in the meniscus area. In this regime, an inversely proportional relationship is manifested between the solid film thickness (h) and coating velocity (U) according to eqn (2):

$$h = \frac{c}{\rho} \frac{Q_{evap}}{W} \frac{1}{U} \tag{2}$$

where ρ and W denote the density and width of the solid film, respectively, Q_{evap}/W represents the evaporation flux per unit length, and U is the coating speed.[23] Conversely, the Landau–Levich regime occurs when the speed is sufficiently high to maintain wet films on the substrate due to the relatively low drying speed in comparison to the coating speed. In this regime, the perovskite film thickness directly correlates to the wet film thickness, which in this case is directly proportional to the speed according to eqn (3):

$$t_{wet} = c_1 L \left(\frac{\mu U}{\gamma}\right)^{2/3} \tag{3}$$

where c_1 is a numerical constant, L is a characteristic length, U is the coating speed, μ is the viscosity, and γ is the surface tension of the solution.[29,39] To meet the industrial throughput demand, scalable linear printing techniques such as blade-coating are required to operate in the Landau–Levich regime, which was found to start at speeds approaching 5 to 10 mm s⁻¹ for one-step blade-coated perovskites.[29,40] As highlighted in eqn (3) and represented in Fig. 3e, increasing the blade speed raises the wet film thickness, which was found to increase the perovskite thickness in one-step blade-coated perovskites.[27,28]

However, in the two-step method, the perovskite thickness is mainly dictated by the amount of pre-deposited PbI₂. Therefore, the classical U-shaped relationship between perovskite thickness and coating speed is not applicable. Instead, due to the heterogeneous nature of the solid/liquid reaction in the hybrid process, it is proposed that increasing the coating speed beyond the critical threshold promotes the diffusion of a larger amount of organohalides throughout the inorganic scaffold *via* the formation of a larger wet film thickness. This mechanism enables precise control over the conversion rate. As a result, it is more insightful to correlate the coating speed with the conversion rate, which is found to follow an S-shape relationship, as represented in Fig. 3e.

It is noteworthy that, unlike the solvent effect, which exhibited divergent trends depending on whether blade-coating or spin-coating was employed as the second step in the hybrid method, the impact of deposition speed remains consistent across both techniques. As previously demonstrated in an earlier work,[12] a systematic increase in spin-coating speed gradually reduces the perovskite conversion rate. This phenomenon occurs because higher speeds result in thinner wet film thicknesses in spin-coating, thereby reducing the
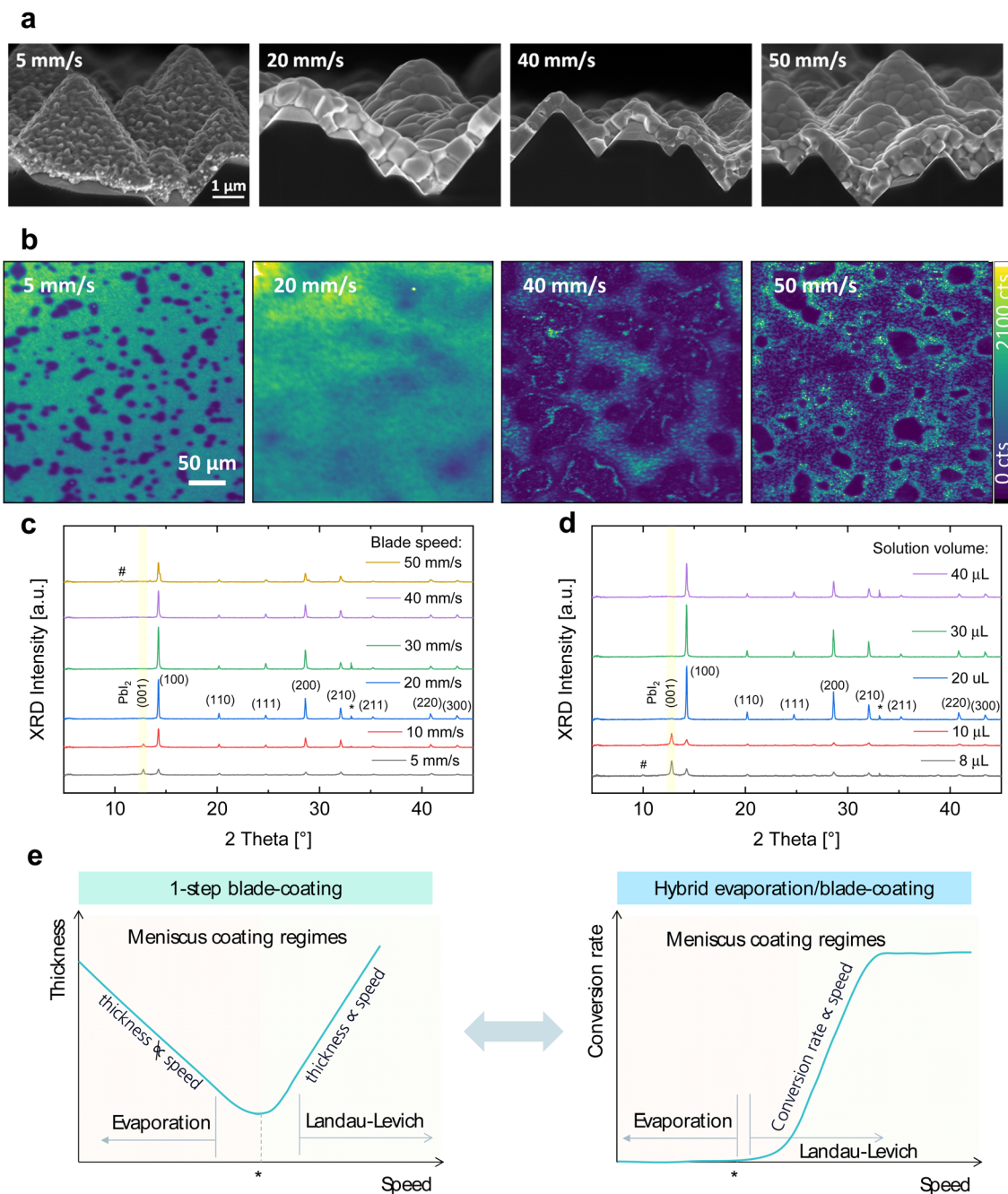
Fig. 3 Impact of blade-coating speed and solution volume on the perovskite's morphological, optoelectronic, and structural properties. (a) Cross-sectional SEM images, (b) 2D PL intensity images taken at the peak energy 1.68 eV from hyperspectral PL measurements, and (c) XRD data of perovskite films fabricated with a variation in blade-coating speed (* Si (002), # δ-perovskite). (d) XRD data of perovskite films with a variation in solution volume (* Si (002), # δ-perovskite). (e) Impact of coating speed on film thickness for meniscus-based films (in this example for one-step blade-coated perovskites) with the two coating regimes namely evaporation and Landau–Levich (adapted from ref. 23), and an analogical equivalent established from our experimental data for perovskite films deposited *via* the hybrid method (* denotes the speed threshold for the transition from evaporation to Landau–Levich regimes).

conversion rate, consistent with the mechanism observed in blade-coating.

We then focused on the coating volume, which is a significant advantage of blade-coating compared to spin-coating, as it consumes nearly ten times less material for the given substrate size of 2.5 × 2.5 cm² in our study. By fixing the coating speed to the optimal value of 20 mm s⁻¹ and studying the impact of the

dispensed volume (from 8 μL to 40 μL), similar observations to the influence of blade speed were found. Specifically, low volumes < 20 μL led to increased densities of residual PbI₂, and perovskite films with high surface roughness and low-crystallinity, whereas higher volumes led to excess organic precursors and deteriorated films (Fig. 3d and S9, ESI†). This can be explained *via* the proportionality between the dispensed

volume, the meniscus height, and the wet film thickness. As the volume of the dispensed solution rises, the meniscus height also rises, which in turn increases the characteristic length (L) according to the formulation in the work of Ernst *et al.*[29] Consequently, the wet film thickness (t_{wet}) increases according to eqn (3), resulting in an enhanced perovskite conversion.

The final critical parameter, stage temperature, has been frequently used in the framework of one-step blade-coated perovskites, with temperatures up to 145 °C, to assist in perovskite crystallization.[41] As shown in Fig. 4, with the hybrid evaporation/blade-coating method, we found that increasing the stage temperature beyond 25 °C resulted in a deterioration of the perovskite film quality. Specifically, the perovskite's apparent grain size decreased, and the roughness of the film increased (Fig. 4a). Furthermore, the PL intensity was significantly quenched (Fig. 4b), with spatial inhomogeneity becoming evident at 80 °C, where bright spots likely originate from the PbI_2-induced passivation effect.[12] Additionally, the absorber's crystallinity and phase purity were compromised (Fig. 4c). The optimal film properties at room temperature are attributed to the lower solvent evaporation rate prolonging the infiltration process and thus improving the conversion rate. Conversely, at high temperature, the solute transport across the thick scaffold is limited by the quick drying dynamics which leads to solute precipitation and reduces structural quality.

Overall, the mechanistic insights revealed through the investigation of parameters involved in the blade-coating step of the hybrid evaporation/blade-coating route suggest a common link between most of the probed parameters and the final perovskite film quality, which are solvent's evaporation rate and wet film thickness. Decreasing the evaporation rate and increasing the wet film thickness through (1) opting for a high boiling point solvent, (2) not introducing gas-quenching (note here that blade-coating was in the glovebox), (3) maintaining the stage at room temperature, (4) increasing the coating speed and (5) the solution volume towards an optimal value, respectively, enables an adequate organohalide solution infiltration through the scaffold which guarantees a full perovskite conversion and a high film crystallinity. These material properties are crucial pre-requisites for optimal charge transport along the absorber and charge transfer across the interface.

2.3 Photovoltaic performance of perovskite single junction and perovskite/silicon tandem solar cells

To evaluate the effectiveness of the developed perovskite film with the hybrid evaporation/blade-coating method on device
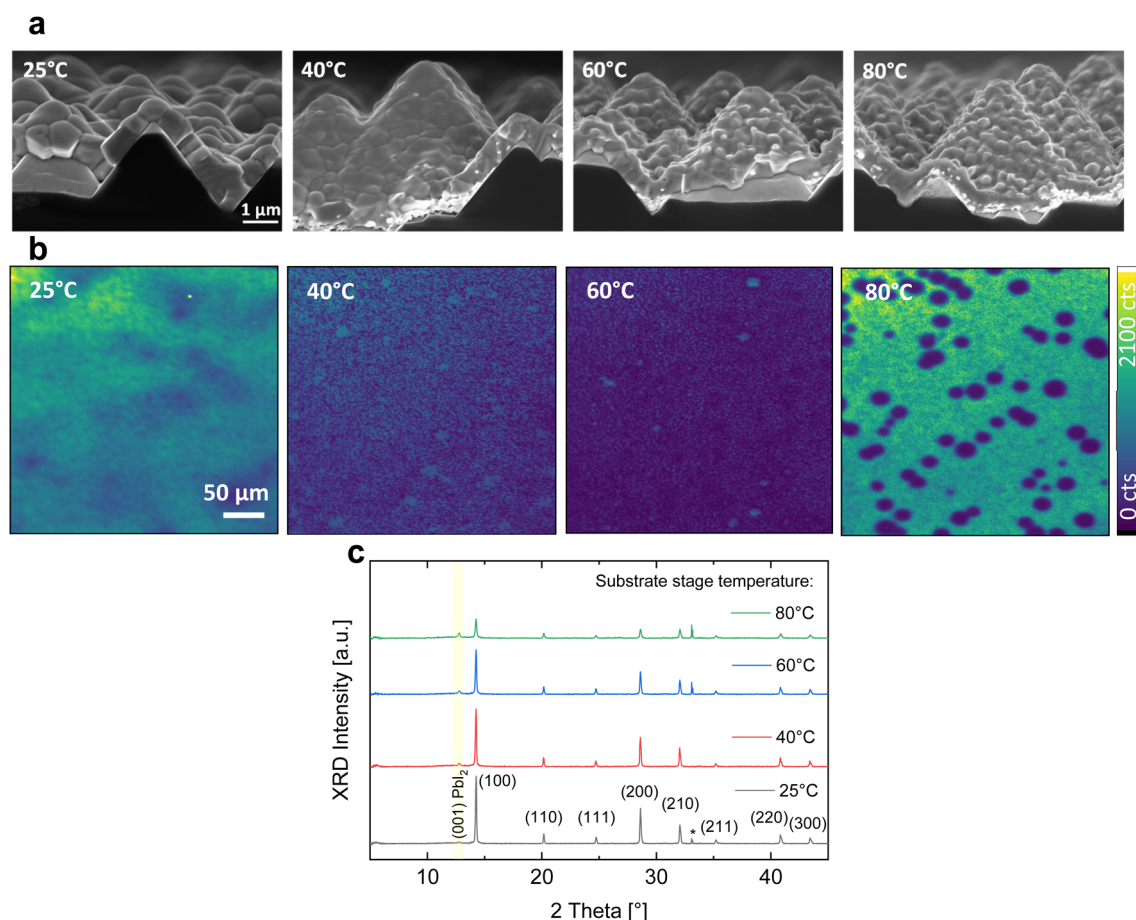

Fig. 4 Impact of stage temperature on the perovskite's morphological, optoelectronic, and structural properties. (a) Cross-sectional SEM images, (b) 2D PL intensity images taken at the peak energy 1.68 eV from hyperspectral PL measurements, and (c) XRD data of perovskite films fabricated with a variation in blade-coating speed (* (002) Si).

level, we first prepared perovskite single junction solar cells on ohmic textured silicon substrates in the p–i–n architecture with 1.04 cm² active area (Fig. 5). The ohmic silicon substrates, which are not photoactive, provide the textured morphology similar to fully-textured tandem solar cells, allowing for a direct assessment of the photovoltaic metrics of the perovskite single
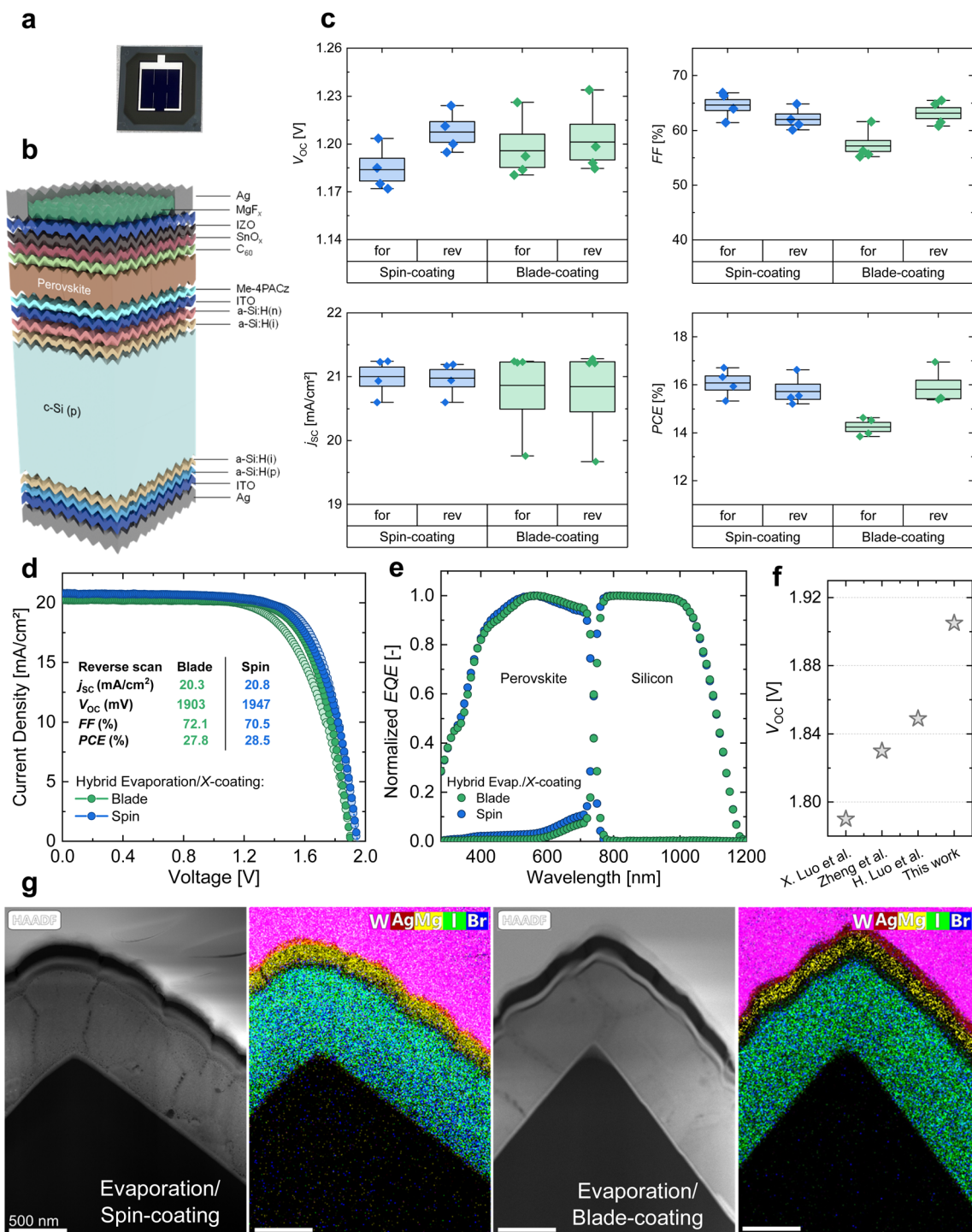
Fig. 5 Photovoltaic performance of single junction and tandem solar cells. (a) Photograph of the tandem solar cell. (b) Schematic of the tandem solar cell architecture. (c) Box plot depicting the *jV* photovoltaic parameters of perovskite single junction solar cells fabricated on ohmic textured silicon substrates (similar architecture as in (b)) but without a photoactive silicon sub-cell (here the silicon is only used to provide the textured substrate morphology), and with a variation in the wet-chemical step of the hybrid method (blade-coating *vs.* spin-coating). (d) *jV* Curves with reverse scan data, and (e) normalized EQE spectra of champion fully-textured perovskite/silicon tandem solar cells using hybrid method with a variation in the wet-chemical step (blade-coating *vs.* spin-coating). (f) Evolution of V_{OC} in reported perovskite/silicon publications using the hybrid evaporation/blade-coating method for perovskite fabrication.[19,42,43] (g) STEM images of perovskite/silicon tandem solar cells fabricated with either hybrid evaporation/spin-coating or hybrid evaporation/blade-coating.

junction solar cell. As a reference, perovskite films were fabricated with the established hybrid evaporation/spin-coating route.

Using the hybrid evaporation/blade-coating method, perovskite single junction solar cells on ohmic textured silicon substrates with 1.04 cm^2 active area delivered an average open-circuit voltage (V_{OC}) of 1199 mV, with a champion value of 1230 mV (Fig. 5c). This performance slightly surpassed that of reference devices with spin-coating counterpart, which exhibited an average V_{OC} of 1196 mV and a maximum value of 1214 mV. Additionally, the short-circuit current density (j_{SC}) in the best-performing devices was comparable to the reference at 21.2 mA cm^{-2} (Fig. 3c). However, a strong hysteresis was observed in the fill factor (FF), resulting in a lower average value of 60.2% compared to 63.3% for cells using the hybrid evaporation/spin-coating method. Ultimately, the average PCE of single junction solar cells with blade-coating was 15.0%, with the champion device achieving 16.6% in the forward scan and 17.0% in the reverse scan. On the other hand, cells using spin-coating as the wet-chemical method demonstrated an average PCE of 15.9%, with the champion device delivering 16.7% in the forward scan and 16.6% in the reverse scan, highlighting the competitive PCE achieved using the scalable hybrid method. The champion devices showed a stable power output at MPP (Fig. S10, ESI†).

In a final step, the developed perovskite preparation method was transferred to fully functional silicon bottom solar cells (jV curve of the sub-cell in a single-junction configuration shown in Fig. S10, ESI†). A champion device was fabricated reaching 27.8% PCE and 1903 mV V_{OC} (reverse scan). This voltage aligned with results from single-junction solar cells on ohmic textured silicon substrates, comprising approximately 1200 mV from the perovskite sub-cell and nearly 700 mV from the silicon sub-cell. Notably, it represents a 50 mV enhancement over previously established fully-textured tandem solar cells using a scalable perovskite deposition method (Fig. 5f).[19,42,43] The high V_{OC} attests to the low non-radiative recombination in the perovskite stack. We attribute this mainly to the homogeneous halide homogeneity, as evidenced by elemental mapping *via* scanning transmission electron microscopy (STEM) combined with energy-dispersive X-ray spectroscopy (STEM-EDX), which show a level of uniformity comparable to that of the reference film produced *via* hybrid evaporation/spin-coating (Fig. 5g). Similarly, the crystallinity of the optimized perovskite film appears similar between both perovskites as can be seen through grazing-incidence wide-angle scattering (GIWAXS) data (Fig. S11, ESI†).

To further enhance device performance, identifying the primary sources of losses within the device is crucial. PL quantum yield (PLQY) analysis using hyperspectral PL indicated an implied V_{OC} (iV_{OC}), also referred to as quasi-Fermi level splitting (QFLS), of 1260 mV for the perovskite half-stack (Fig. S12, ESI†). Extending the analysis to include the C$_{60}$ electron transport layer (ETL) revealed a slight decrease in iV_{OC} to 1230 mV. The 30 mV drop in iV_{OC} highlights low non-radiative recombination at the critical perovskite/C$_{60}$ interface.[2,16,44] This finding suggests that the primary leverage for further

minimizing non-radiative recombination losses lies within the perovskite half-stack. In this context, buried interface engineering strategies, such as incorporation of 2D interlayers, have shown considerable promise.[13,15,45] These approaches not only mitigate photovoltage losses at the hole transport layer (HTL)/perovskite interface, but also enhance perovskite growth, thereby offering viable venues for further improvement of V_{OC}.

Regarding j_{SC}, preliminary estimations based on EQE indicate that the tandem cell is silicon-limited. To address this, future work utilizing this cell structure should focus on either increasing the perovskite bandgap or reducing its thickness to increase the photogenerated current in the silicon sub-cell and tend towards current-matching. The former approach is particularly promising, as increasing the bandgap could also yield additional benefits for V_{OC}, provided that halide segregation challenges are effectively managed. In addition to current-mismatch, parasitic absorption in the functional layers above the perovskite further diminishes the j_{SC} of the device. Among these layers, C$_{60}$ contributes the most significant parasitic absorption,[7] with a numerically estimated current loss of 1.04 mA cm^{-2} for the used 13 nm thickness.[46] By reducing the thickness of the C$_{60}$ layer, absorption in the region below 600 nm can be effectively minimized (Fig. S13, ESI†), thereby enhancing photon absorption in the perovskite absorber. However, the high cost and mechanical reliability concerns associated with C$_{60}$ emphasize the importance of investigating alternative ETLs that are not only optically transparent and mechanically robust, but also deposited with a scalable method. In this context, evaporated electron-selective SAMs or ALD-deposited SnO$_x$ ETLs present promising alternatives.[47,48]

Finally, with regard to the FF, we hypothesize that the absence of a buried interface engineering strategy significantly restricts this jV parameter. Such strategies not only mitigate the valence band energetic offset at the perovskite/HTL interface, but also influence the growth of the perovskite film, ultimately enhancing its material quality. To get insights into the energetic alignment, we conducted photoelectron spectroscopy in air (PESA) measurements on stacks comprising textured silicon/ITO/Me-4PACz both with and without the perovskite layer (Fig. S14, ESI†). These measurements revealed a substantial 170 meV difference between the valence band maximum (VBM) of the perovskite film and the highest occupied molecular orbital (HOMO) of the HTL (Me-4PACz). Based on this finding, the use of self-assembled monolayers (SAMs) with a more aligned HOMO level and/or the introduction of a 2D interlayer with compatible energy levels are anticipated to improve the FF of the device.[13,15,28,49]

In a final step, we tested the stability of the developed tandem solar cell. Devices were aged for 1680 hours without encapsulation, in inert atmosphere (glovebox), without electrical or light bias during storage. This test corresponds to the ISOS-D-1I standard (level 1 of dark storage studies for intrinsic stability testing) in the consensus statement based on the ISOS procedures.[50] In this test, the devices showed minimal degradation in all the jV metrics, retaining up to 99.8% of their initial PCE (Fig. S15, ESI†).

Then, we encapsulated one of these devices and performed an outdoor stability test, in the desertic climate of the Red Sea coast. Here, all quadrants of the operational conditions such as continuous operation under illumination and heat, alongside diurnal heat cycles, were present. The daily peak device temperature reached values of up to 40 °C and the light intensity on a sunny day reached 1.26 suns (measured by a pyranometer) at noon. In this test, the device exhibited a more pronounced degradation (Fig. S16, ESI†). Specifically, the I_{SC} decreased by 22.1%, the V_{OC} declined by 10.2%, and the FF dropped by 42.5%, relative to their initial values. Consequently, the PCE of the devices fell to 45% by the end of the testing period.

The assessment of the stability of tandem solar cells with scalable perovskite fabrication outdoors is crucial for identifying the current status of the technology. To the best of our knowledge, this study marks the first outdoor test of a fully-textured tandem solar cell featuring a perovskite film produced via a scalable method. The result of the test underlines the critical need for R&D optimization targeted towards not only efficiency, but also stability, at initial stages of development. By providing a comprehensive understanding of the coating dynamics using the hybrid evaporation/blade-coating method in this work, future studies will involve compositional engineering to enhance the intrinsic stability of the perovskite absorber. This, together with solving the engineering challenges of scaling the deposition area, and enhancement of throughput, constitute promising avenues for advancing the technology towards its commercialization.

3. Conclusion

In summary, this study elucidated the coating dynamics involved in the hybrid evaporation/blade-coating route, facilitating the control of perovskite film growth on textured silicon with large pyramid height. By identifying key mechanistic factors, such as the solvent's evaporation rate and the wet film thickness, various perovskite film properties—including conversion rate, grain size, and surface roughness—were effectively regulated. Regarding blade speed, unlike one-step blade-coated perovskites where increased speed results in a U-shaped speed-dependent thickness for evaporation and Landau–Levich regimes, the hybrid method uncovered a different S-shaped curve correlating speed with perovskite conversion rate. The study further highlighted both the parallels and distinctions between the scalable evaporation/blade-coating method and the well-established evaporation/spin-coating route. It emphasized the importance of prioritizing scalable fabrication methods at early stages of R&D and focusing not on PCE enhancement but also on operational stability. By systematically studying the coating dynamics in the blade-coating step, a fully-textured perovskite/silicon tandem solar cell was developed, achieving a V_{OC} of 1903 mV and a PCE of approximately 28%. Remarkably, this was accomplished with a solution volume that was eight times lower than that used in the hybrid evaporation/spin-coating method.

Data availability

The data supporting this article have been included as part of the ESI.†

Author contributions

O. E. conceived the project idea and coordinated the work. O. E. carried out the process parameter investigations, fabricated single-junction solar cells, performed film analysis and device characterization (XRD, SEM, GIWAXS, hyperspectral PL, and jV), and wrote the first draft of the manuscript. A. A. S., V. H. and A. S. S. fabricated the tandem solar cells. A. A. S. carried out jV and EQE characterization of the tandem solar cells and supported with SEM and XRD characterization. V. H. supported with hyperspectral PL and performed PLQY analysis, as well as supported with fabrication of film stacks. B. V. performed the STEM measurements. A. R. P. performed PESA measurements. M. M. performed the outdoor stability measurements. M. B. provided the silicon bottom solar cells and A. R. P. contributed to the preparation of Si cells. A. S. S. made most of the schematics of the manuscript. A. S. S., M. K., J. B., P. S.C. S., S. D. W. and S. G. supervised the overall project and secured the funding. All authors reviewed the manuscript and repeatedly helped with manuscript reviews.

Conflicts of interest

There are no conflicts to declare.

Acknowledgements

References

1 J. Liu, Y. He, L. Ding, H. Zhang, Q. Li, L. Jia, J. Yu, T. W. Lau, M. Li, Y. Qin, X. Gu, F. Zhang, Q. Li, Y. Yang, S. Zhao, X. Wu, J. Liu, T. Liu, Y. Gao, Y. Wang, X. Dong, H. Chen, P. Li, T. Zhou, M. Yang, X. Ru, F. Peng, S. Yin, M. Qu, D. Zhao, Z. Zhao, M. Li, P. Guo, H. Yan, C. Xiao, P. Xiao, J. Yin, X. Zhang, Z. Li, B. He and X. Xu, *Nature*, 2024, **635**, 596–603.
2 S. Mariotti, E. Köhnen, F. Scheler, K. Sveinbjörnsson, L. Zimmermann, M. Piot, F. Yang, B. Li, J. Warby, A. Musiienko, D. Menzel, F. Lang, S. Keßler, I. Levine, D. Mantione, A. Al-Ashouri, M. S. Härtel, K. Xu, A. Cruz, J. Kurpiers, W. P. Wagner, H. Köbler, J. Li, A. Magomedov, D. Mecerreyes, E. Unger, A. Abate, M. Stolterfoht,

B. Stannowski, R. Schlatmann, L. Korte and S. Albrecht, *Science*, 2023, **381**, 63–69.

3 E. Ugur, A. A. Said, P. Dally, S. Zhang, C. E. Petoukhoff, D. R. Villalva, S. Zhumagali, B. K. Yildirim, A. Razzaq, S. Sarwade, A. Yazmaciyan, D. Baran, F. Laquai, C. Deger, I. Yavuz, T. G. Allen, E. Aydin and S. de Wolf, *Science*, 2024, **385**, 533–538.

4 F. Gota, R. Schmager, A. Farag and U. W. Paetzold, *Opt. Express*, 2022, **30**, 14172–14188.

5 J. Lehr, M. Langenhorst, R. Schmager, S. Kirner, U. Lemmer, B. S. Richards, C. Case and U. W. Paetzold, *Sustainable Energy Fuels*, 2018, **8**, 506.

6 N. Tucher, O. Höhn, J. N. Murthy, J. C. Martinez, M. Steiner, A. Armbruster, E. Lorenz, B. Bläsi, J. C. Goldschmidt, N. Tucher, J. C. Martinez, M. Steiner and J. C. Goldschmidt, *Opt. Express*, 2019, **27**, A1419.

7 O. Er-raji, C. Messmer, A. J. Bett, O. Fischer, S. K. Reichmuth, F. Schindler, M. Bivour, O. Schultz-Wittmann, J. Borchert, M. Hermle, J. Schön, F. D. Heinz, M. C. Schubert, P. S. C. Schulze and S. W. Glunz, *Sol. RRL*, 2023, **7**, 2300659.

8 L. Xu, J. Liu, K. McIntosh, M. Abbott, E. Aydin, T. Allen, M. de Bastiani, M. Babics, J. Kang, M. Alamer, W. Yan, W. Liu, F. Xu, A. u. Rehman and S. de Wolf, *PRX Energy*, 2022, **1**, 023005.

9 T. Yang, L. Mao, J. Shi, P. Zeng, F. Li, J. Gong, X. Huang, Z. Wang, W. Cui, D. Huang, H. Zhang, Y. Sun, X. Fang, Z. Liu, M. Liu and X. Cui, *Adv. Energy Mater.*, 2023, 2303149.

10 Q. Xu, B. Shi, Y. Li, J. Liu, Y. Li, Z. SunLi, P. Liu, Y. Zhang, C. Sun, W. Han, Q. Huang, D. Zhang, H. Ren, X. Du, Y. Zhao and X. Zhang, *Adv. Mater.*, 2023, e2308692.

11 Y. Li, B. Shi, Q. Xu, L. Yan, N. Ren, Y. Chen, W. Han, Q. Huang, Y. Zhao and X. Zhang, *Adv. Energy Mater.*, 2021, **11**, 2102046.

12 O. Er-raji, A. Bett, S. Lange, H. Nagel, M. Bivour, O. Schultz-Wittmann, C. Hagendorf, M. Hermle, J. Borchert, S. Glunz and P. Schulze, *Prog. Photovoltaics*, 2023, **33**, 1–14, https://onlinelibrary.wiley.com/doi/10.1002/pip.3770.

13 F. Zhang, B. Tu, S. Yang, K. Fan, Z. Liu, Z. Xiong, J. Zhang, W. Li, H. Huang, C. Yu, A. K-Y Jen and K. Yao, *Adv. Mater.*, 2023, **35**, e2303139.

14 Q. Xu, B. Shi, Y. Li, L. Yan, W. Duan, Y. Li, R. Li, N. Ren, W. Han, J. Liu, Q. Huang, D. Zhang, H. Ren, S. Xu, C. Zhang, H. Zhuang, A. Lambertz, K. Ding, Y. Zhao and X. Zhang, *Adv. Energy Mater.*, 2022, **12**, 2202404.

15 Z. Liu, Z. Xiong, S. Yang, K. Fan, L. Jiang, Y. Mao, C. Qin, S. Li, L. Qiu, J. Zhang, F. R. Lin, L. Fei, Y. Hua, J. Yao, C. Yu, J. Zhou, Y. Chen, H. Zhang, H. Huang, A. K.-Y. Jen and K. Yao, *Joule*, 2024, **8**, 2834–2850.

16 X. Y. Chin, D. Turkay, J. A. Steele, S. Tabean, S. Eswara, M. Mensi, P. Fiala, C. M. Wolff, A. Paracchino, K. Artuk, D. Jacobs, Q. Guesnay, F. Sahli, G. Andreatta, M. Boccard, Q. Jeangros and C. Ballif, *Science*, 2023, **381**, 59–63.

17 J. Chen, S. Yang, L. Jiang, K. Fan, Z. Liu, W. Liu, W. Li, H. Huang, H. Zhang and K. Yao, *Angew. Chem., Int. Ed. Engl.*, 2024, **63**, e202407151.

18 O. Er-raji, S. Lange, C. E. Hartwig, A. Prasetio, M. Bivour, M. Hermle, M. Turek, S. de Wolf, S. W. Glunz, J. Borchert and P. S. C. Schulze, *Small Methods*, 2025, e2401758.

19 X. Zheng, W. Kong, J. Wen, J. Hong, H. Luo, R. Xia, Z. Huang, X. Luo, Z. Liu, H. Li, H. Sun, Y. Wang, C. Liu, P. Wu, H. Gao, M. Li, A. D. Bui, Y. Mo, X. Zhang, G. Yang, Y. Chen, Z. Feng, H. T. Nguyen, R. Lin, L. Li, J. Gao and H. Tan, *Nat. Commun.*, 2024, **15**, 4907.

20 G. Shi, Z. Huang, R. Qiao, W. Chen, Z. Li, Y. Li, K. Mu, T. Si and Z. Xiao, *Nat. Commun.*, 2024, **15**, 1066.

21 W. Shen, H. Fang, D. Pu, W. Zheng, X. Zhang, G. Li, L. Huang, S. Zhou, W. Chen, Y. Zhou, Z. Feng, J. Liang, J. Zhou, P. Qin, G. Fang and W. Ke, *Adv. Energy Mater.*, 2024, 2410605.

22 H. Fang, W. Shen, H. Guan, G. Chen, G. Li, W. Ai, S. Fu, Z. Xu, W. Chen, P. Jia, Z. Yu, S. Wang, Z. Yu, Q. Lin, J. Wang, J. Zheng, D. Pu, G. Fang and W. Ke, *Adv. Mater.*, 2024, 2414790.

23 C. Huang, S. Tan, B. Yu, Y. Li, J. Shi, H. Wu, Y. Luo, D. Li and Q. Meng, *Joule*, 2024, **8**, 2539–2553.

24 M. Kohlstädt, M. A. Yakoob and U. Würfel, *Phys. Status Solidi A*, 2018, **26**, 3.

25 G. Chen, S. Wang, Z. Yu, C. Dong, P. Jia, D. Pu, K. Dong, H. Cui, H. Fang, C. Wang, R. Gao, F. Yao, W. Ke, G. Li and G. Fang, *Sci. Bull.*, 2024, 212–222.

26 B. Chen, Z. J. Yu, S. Manzoor, S. Wang, W. Weigand, Z. Yu, G. Yang, Z. Ni, X. Dai, Z. C. Holman and J. Huang, *Joule*, 2020, 850–864.

27 K.-W. Huang, M.-H. Li, Y.-T. Chen, Z.-X. Wen, C.-F. Lin and P. Chen, *J. Mater. Chem. C*, 2024, **12**, 1533–1542.

28 A. S. Subbiah, L. V. Torres Merino, A. R. Pininti, V. Hnapovskyi, S. Mannar, E. Aydin, A. Razzaq, T. G. Allen and S. de Wolf, *ACS Energy Lett.*, 2024, **9**, 727–731.

29 M. Ernst, J.-P. Herterich, C. Margenfeld, M. Kohlstädt and U. Würfel, *Sol. RRL*, 2021, 2100535.

30 H. S. Lee, M. K. Kim, S. R. Pae, D. Kim, H. Seo, P. Boonmongkolras, I. Gereige, S. Park and B. Shin, *Nano Energy*, 2020, **74**, 104830.

31 M. K. Kim, H. S. Lee, S. R. Pae, D.-J. Kim, J.-Y. Lee, I. Gereige, S. Park and B. Shin, *J. Mater. Chem. A*, 2018, **6**, 24911–24919.

32 M. A. A. Mahmoud, O. Er-raji, B. P. Kore, M. Bivour, P. S. C. Schulze, S. W. Glunz, A. W. Bett and J. Borchert, *Sol. RRL*, 2024, **8**, 2400471.

33 O. Er-raji, M. A. Mahmoud, O. Fischer, A. J. Ramadan, D. Bogachuk, A. Reinholdt, A. Schmitt, B. P. Kore, T. W. Gries, A. Musiienko, O. Schultz-Wittmann, M. Bivour, M. Hermle, M. C. Schubert, J. Borchert, S. W. Glunz and P. S. Schulze, *Joule*, 2024, **8**, 2811–2833.

34 B. Roose, K. Dey, Y.-H. Chiang, R. H. Friend and S. D. Stranks, *J. Phys. Chem. Lett.*, 2020, **11**, 6505–6512.

35 Y. Gao, H. Raza, Z. Zhang, W. Chen and Z. Liu, *Adv. Funct. Mater.*, 2023, **33**, 2215171.

36 O. Er-raji, L. Rustam, B. P. Kore, S. W. Glunz and P. S. C. Schulze, *ACS Appl. Energy Mater.*, 2023, **6**, 6183–6193.

37 J. Yang, E. L. Lim, L. Tan and Z. Wei, *Adv. Energy Mater.*, 2022, **12**, 2200975.

38 L. D. Landau and B. Levich, *Acta Physicochim*, URSS, 1942.

39 S. Siegrist, P. Nandi, R. K. Kothandaraman, A. Abdessalem, A. N. Tiwari and F. Fu, *Sol. RRL*, 2023, **7**, 2300273.

40 Y. Deng, X. Zheng, Y. Bai, Q. Wang, J. Zhao and J. Huang, *Nat. Energy*, 2018, **3**, 560–566.

41 R. Wu, C. Wang, M. Jiang, C. Liu, D. Liu, S. Li, Q. Kong, W. He, C. Zhan, F. Zhang, X. Liu, B. Yang and W. Hu, *J. Renewable Sustainable Energy*, 2021, **13**, 012701.

42 X. Luo, H. Luo, H. Li, R. Xia, X. Zheng, Z. Huang, Z. Liu, H. Gao, X. Zhang, S. Li, Z. Feng, Y. Chen and H. Tan, *Adv. Mater.*, 2023, **35**, e2207883.

43 H. Luo, X. Zheng, W. Kong, Z. Liu, H. Li, J. Wen, R. Xia, H. Sun, P. Wu, Y. Wang, Y. Mo, X. Luo, Z. Huang, J. Hong, Z. Chu, X. Zhang, G. Yang, Y. Chen, Z. Feng, J. Gao and H. Tan, *ACS Energy Lett.*, 2023, **8**, 4993–5002.

44 J. Liu, M. de Bastiani, E. Aydin, G. T. Harrison, Y. Gao, R. R. Pradhan, M. K. Eswaran, M. Mandal, W. Yan, A. Seitkhan, M. Babics, A. S. Subbiah, E. Ugur, F. Xu, L. Xu, M. Wang, A. u. Rehman, A. Razzaq, J. Kang, R. Azmi, A. A. Said, F. H. Isikgor, T. G. Allen, D. Andrienko, U. Schwingenschlögl, F. Laquai and S. de Wolf, *Science*, 2022, **377**, 302–306.

45 A. S. Subbiah, S. Mannar, V. Hnapovskyi, A. R. Pininti, B. Vishal, L. V. Torres Merino, O. Matiash, O. Karalis, H. Hempel, A. Prasetio, B. Yildirim, P. Dally, D. Rosas Villalva, M. Babics, L. Xu, A. Razzaq, R. Azmi, F. Xu, H. L. Bristow, E. Ugur, A. Ur Rehman, H. Pasanen, E. Aydin, T. Allen, D. Baran, T. Unold, F. Laquai and S. de Wolf, *Joule*, 2024, 101767.

46 V. Sittinger, P. S. C. Schulze, C. Messmer, A. Pflug and J. C. Goldschmidt, *Opt. Express*, 2022, **30**, 37957–37970.

47 D. Gao, B. Li, Q. Liu, C. Zhang, Z. Yu, S. Li, J. Gong, L. Qian, F. Vanin, K. Schutt, M. A. Davis, A. F. Palmstrom, S. P. Harvey, N. J. Long, J. M. Luther, X. C. Zeng and Z. Zhu, *Science*, 2024, **386**, 187–192.

48 J. Suo, B. Yang, D. Bogachuk, G. Boschloo and A. Hagfeldt, *Adv. Energy Mater.*, 2024, 2400205.

49 L. V. Torres Merino, C. E. Petoukhoff, O. Matiash, A. S. Subbiah, C. V. Franco, P. Dally, B. Vishal, S. Kosar, D. Rosas Villalva, V. Hnapovskyi, E. Ugur, S. Shah, F. Peña Camargo, O. Karalis, H. Hempel, I. Levine, R. R. Pradhan, S. Kralj, N. Kalasariya, M. Babics, B. K. Yildirim, A. A. Said, E. Aydin, H. Bristow, S. Mannar, W. Raja, A. R. Pininti, A. Prasetio, A. Razzaq, H. Al Nasser, T. G. Allen, F. H. Isikgor, D. Baran, T. D. Anthopoulos, M. M. Masis, U. Schwingenschlögl, T. Unold, M. Stolterfoht, F. Laquai and S. de Wolf, *Joule*, 2024, **8**, 2585–2606.

50 M. V. Khenkin, E. A. Katz, A. Abate, G. Bardizza, J. J. Berry, C. Brabec, F. Brunetti, V. Bulović, Q. Burlingame, A. Di Carlo, R. Cheacharoen, Y.-B. Cheng, A. Colsmann, S. Cros, K. Domanski, M. Dusza, C. J. Fell, S. R. Forrest, Y. Galagan, D. Di Girolamo, M. Grätzel, A. Hagfeldt, E. v. Hauff, H. Hoppe, J. Kettle, H. Köbler, M. S. Leite, S. Liu, Y.-L. Loo, J. M. Luther, C.-Q. Ma, M. Madsen, M. Manceau, M. Matheron, M. McGehee, R. Meitzner, M. K. Nazeeruddin, A. F. Nogueira, Ç. Odabaşı, A. Osherov, N.-G. Park, M. O. Reese, F. de Rossi, M. Saliba, U. S. Schubert, H. J. Snaith, S. D. Stranks, W. Tress, P. A. Troshin, V. Turkovic, S. Veenstra, I. Visoly-Fisher, A. Walsh, T. Watson, H. Xie, R. Yıldırım, S. M. Zakeeruddin, K. Zhu and M. Lira-Cantu, *Nat. Energy*, 2020, **5**, 35–49, https://www.nature.com/articles/s41560-019-0529-5.pdf.